Insulator-metal transitions in the T phase Cr-doped and $M1$ phase undoped VO_2 thin films

S. S. Majid,[1] D. K. Shukla,[2,*] F. Rahman,[1] S. Khan,[3] K. Gautam,[2] A. Ahad,[1] S. Francoual,[4] R. J. Choudhary,[2] V. G. Sathe,[2] and J. Strempfer[4,5]

[1]*Department of Physics, Aligarh Muslim University, Aligarh 202002, India*
[2]*UGC-DAE Consortium for Scientific Research, Indore 452001, India*
[3]*Nano Science Lab, Materials Science Division, Raja Ramanna Centre for Advanced Technology, Indore 452013, India*
[4]*Deutsches Elektronen-Synchrotron (DESY), Notkestrasse 85, D-22607 Hamburg, Germany*
[5]*Advanced Photon Source, Argonne National Laboratory, Argonne, Illinois 60439, USA*

(Received 25 September 2017; revised manuscript received 30 July 2018; published 28 August 2018)

VO_2 exhibits several insulating phases (monoclinic $M1$, $M2$, and triclinic T), and the study of these phases is important for understanding the true nature of the insulator-to-metal transition (IMT) in VO_2. These insulating phases have small but discernible crystallographic differences in the vanadium chains forming the dimers. Peculiarities of the electron localizations in the dimerized chains for many of the probes such as NMR make it difficult to characterize the true character of these phases [T. J. Huffman *et al.*, Phys. Rev. B **95**, 075125 (2017); J. Pouget *et al.*, Phys. Rev. B **10**, 1801 (1974)]. Here we present structural, electrical, ultrafast-reflectivity, and electronic structure studies of the T phase Cr-doped VO_2 and the $M1$ phase pure VO_2 thin films, both grown by pulsed laser deposition under identical conditions. An intermediate $M2$ structure is observed in the Cr-doped VO_2, while the pure VO_2 directly goes from the insulating monoclinic $M1$ structure to a metallic rutile R structure, manifested by temperature-dependent Raman spectroscopy. Temperature-dependent electronic structure studies utilizing x-ray near-edge absorption spectroscopy reveal that all these insulating phases (monoclinic $M1$ and $M2$ and triclinic T) have similar electronic structures which place these insulating phases into the list of Mott-Hubbard insulators. This is a first combined experimental report on the electronic structure of all the three insulating phases, monoclinic $M1$, $M2$, and triclinic T.

DOI: 10.1103/PhysRevB.98.075152

I. INTRODUCTION

Vanadium oxides, belonging to the Magnéli phases, have been extensively studied because of their insulator-to-metal transition (IMT), which is accompanied by a huge and abrupt change in the electrical properties at the transition [1]. Vanadium dioxide, VO_2, undergoes a first-order transition from a low-temperature insulating monoclinic $M1$ phase ($P2_1/c$) to a high-temperature metallic rutile R phase ($P4_2/mnm$), with a transition temperature T_c around 340 K [1,2]. In the R phase, the V atoms are equally spaced along the rutile c axis, while in the $M1$ phase simultaneous pairing and tilting among V atoms occur, leading to a zigzag pattern [3,4].

In the VO_2, doping has been found to be extremely useful to tune the IMT temperature and associated thermochromic properties and to study the Mott and Peierls physics [5,6]. Doping of acceptor impurities, viz., Al and Cr, leads to several insulating phases with similar free energies which can be controlled by doping concentration or strain [3,7,8]. Cr doping in VO_2 produces structural modifications with low impact on electrical conductivity [3]. The insulating phases monoclinic $M2$ and triclinic T are observed at very low Cr concentrations [3,8,9]. In the $M2$ phase, only one half of the V atoms dimerize along the c axis, and the other half forms zigzag chains of equally spaced atoms, while the T phase has V-V pairs of $M2$ tilt and zigzag chains start to pair [3]. From the structural point of view, the T phase occurs in between the $M1$ and $M2$ phases, and an almost continuous transition from the T phase to the $M1$ phase has been observed on decreasing the temperature, without the involvement of the latent heat, which is in contrast to the first-order transition between the $M2$ and T phases [3,9–11].

In VO_2 the electron-lattice interactions and the electron-electron correlations both play an important role in the IMT [12–14]. Most of the scientific interest is focused on understanding the role and relative importance of the electron-electron correlations (Mott-Hubbard model) and the electron-lattice interactions (Peierls model) in the IMT [15,16]. VO_2 insulating phases ($M1$, T, and $M2$) with different vanadium dimers will have different intradimer hopping parameters t, and based on the competition between the intra-dimer Coulomb repulsion U and the hopping parameter t, the Peierls ($U \ll t$) and Mott-Hubbard ($U \gg t$) pictures are considered the limiting cases [2,17]. Recently, Huffman *et al.* [10], using optical spectroscopy, showed that the energy band gaps of all these VO_2 insulating phases ($M1$, T, and $M2$) are similar and primarily arise due to the dominating intra-dimer Coulomb repulsion ($U \gg t$). In this scenario, studying the electronic structure of all the insulating phases of VO_2 is important to disentangle the role and relevance of the Peierls and Mott-Hubbard mechanisms.

We synthesized pure and Cr-doped VO_2 thin films on the Si substrate using the pulsed-laser-deposition technique. The VO_2 thin film stabilizes in the monoclinic $M1$ phase, while the Cr-doped thin film has been found to possess the

*dkshukla@csr.res.in

triclinic T phase, as confirmed by x-ray diffraction and Raman measurements. Temperature-dependent resistivity measurements confirm IMT in both the pure and Cr-doped thin films. Temperature-dependent Raman measurements reveal the intermediate $M2$ structure during the transition from the insulating triclinic T structure to the metallic rutile R structure in the doped thin film, contrary to the $M1$ to R transition observed in the pure VO_2 thin film. VO_2 insulating states with different crystal symmetries observed here are also studied with degenerate pump-probe measurements for the study of the dynamics of charge carriers [18–21]. V K-edge x-ray absorption near-edge spectroscopy measurements represent the similar electronic structures of VO_2 $M1$, T, and $M2$ insulating phases.

II. EXPERIMENTAL DETAILS

A KrF excimer laser ($\lambda = 248$ nm, repetition rate of 5 Hz, and pulse energy of 210 mJ) was focused onto a target (pressed pure and Cr-doped V_2O_5) with a fluence of 1.1 mJ/cm^2. The ultrasonically cleaned Si substrate was maintained at a temperature of 700 °C during the deposition. Both depositions were performed in an oxygen partial pressure of 10 mTorr. X-ray diffraction (XRD) was carried out with a Bruker D8 x-ray diffractometer with Cu $K\alpha$ radiation. Temperature-dependent resistivity measurements were performed in the standard four-point configuration. Temperature-dependent Raman spectra were collected in backscattering geometry using a 10-mW Ar (475-nm) laser as an excitation source coupled with a Labram-HRF micro-Raman spectrometer equipped with a 50× objective. The x-ray photoelectron spectroscopy (XPS) measurement was performed using an Omicron energy analyzer (EA-125) with an Al $K\alpha$ (1486.6 eV) x-ray source. Ultrafast reflectivity measurements were performed in a standard degenerate pump-probe geometry with a 100-fs, 82-MHz Ti:sapphire laser. The laser energy was tuned from 1.54 to 1.58 eV. The spectral width of the laser energy at full width at half maximum was nearly 4 meV. The pump and probe beam polarizations were kept orthogonal to minimize coherent artifacts. The laser pump pulse was focused on a sample with a spot size of ∼40 μm, larger than the probe pulse of ∼25 μm. The optical delay in the probe pulse was achieved by a delay stage. A maximum laser power of 300 mW was used during the experiments. The change in the reflectivity ΔR of the sample was measured by chopping the pump and by monitoring the change in the probe intensity using a lock-in amplifier [22]. Temperature-dependent x-ray absorption near-edge spectra (XANES) at the V K edge were measured at beamline P09, PETRA III, DESY, Hamburg, Germany, in fluorescence mode. The angle between the film's surface normal and the incident photon's σ polarization direction was varied using the χ angle of the six-circle diffractometer available in the first experimental hutch [23]. A vanadium metal foil was used as a reference for the purpose of energy calibration. Pre- and postedge corrections of the XAS data were performed using ATHENA software [24].

III. RESULTS

Figure 1(a) shows θ-2θ XRD patterns of the pure and Cr-doped VO_2 thin films deposited under identical conditions.

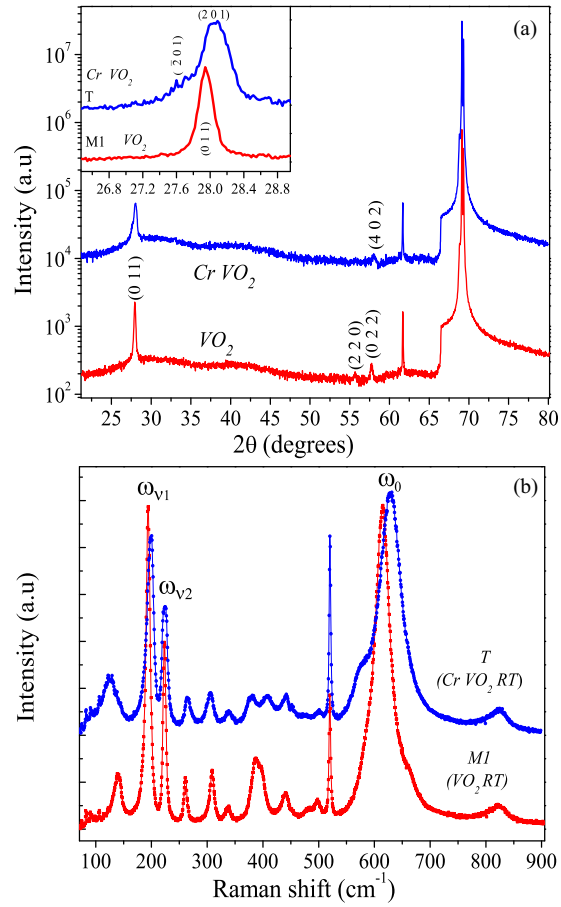

FIG. 1. (a) Room-temperature θ-2θ XRD patterns of the pure and Cr-doped VO_2 thin films on the [001] Si substrate. (b) Room-temperature Raman spectrum of the pure and Cr-doped VO_2 thin films.

The diffraction peaks observed in the pure VO_2 thin film at $2\theta \sim 27.93°$, $55.67°$, and $57.74°$ correspond to the planes (011), (220), and (022), respectively. These represent a stable monoclinic ($M1$) phase of VO_2 (matched with Joint Committee for Powder Diffraction Standard number 82-0661). A zoomed-in view of the (011) reflection of the pure VO_2 and corresponding reflections in the Cr-doped VO_2 are shown in the inset of Fig. 1. The twin peaks at $2\theta \sim 27.56°$ and $28.06°$ observed in the Cr-doped thin film correspond to the (-201) and (201) planes of the T phase, which has the same space group as the $M2$ phase [3,9,25]. The reflection at $2\theta \sim 58.04°$ in the Cr-doped thin film is from the (402) plane of the VO_2 T phase. It should be mentioned here that, normally, XRD cannot unambiguously distinguish between the T and $M2$ phases as there is only a volume discontinuity between these two and the overall structure and space group are the same [7,26]. The thin film nature of our samples makes it even more complicated to make a clear distinction between T and $M2$ phases from the x-ray diffraction data. Raman spectroscopy has been found to be effective for distinguishing between the VO_2 insulating structures. Figure 1(b) shows the room-temperature Raman spectra of pure and Cr-doped VO_2 thin films with the phonon modes belonging to the $M1$ and T structures of VO_2, respectively.

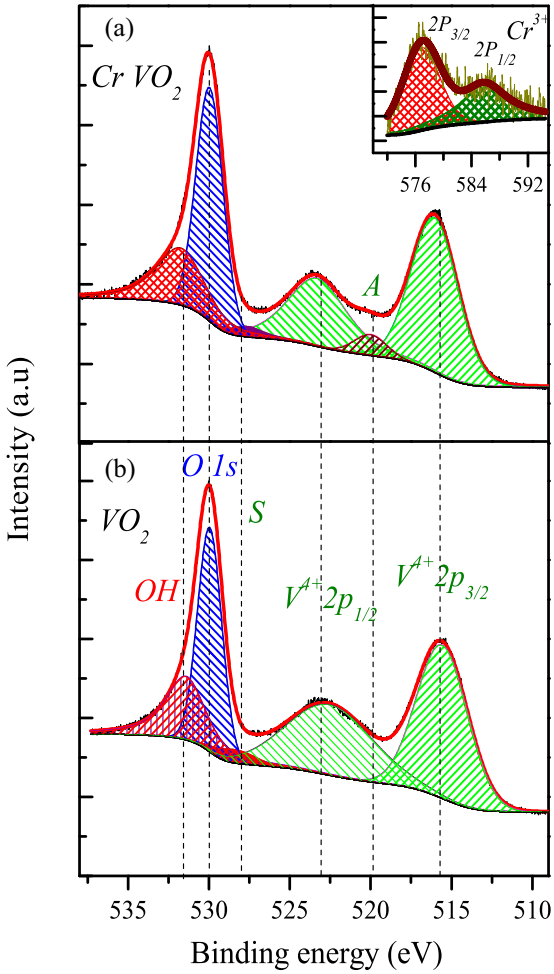

FIG. 2. XPS spectra of (a) Cr-doped and (b) pure VO_2 thin films. The inset shows Cr 2p XPS.

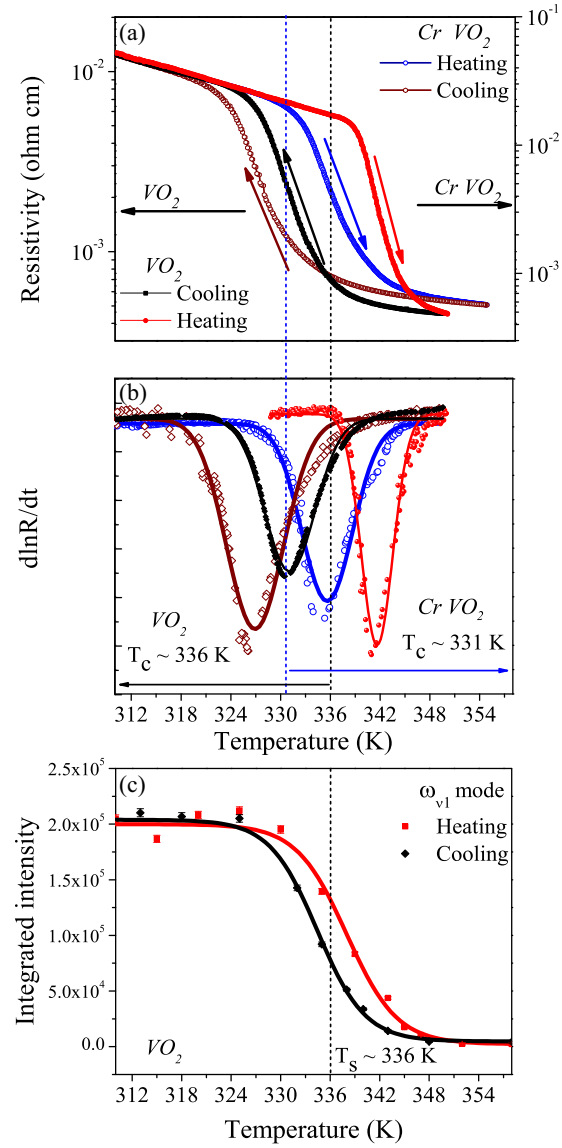

FIG. 3. (a) Temperature-dependent resistivity of the pure and Cr-doped VO_2 thin film. (b) Gaussian fitting of the differential curves of resistivity vs temperature. (c) Temperature-dependent integrated intensity of the Raman ω_{v_1} phonon mode for cooling and heating cycles in the VO_2 thin film.

The T structure in the Cr-doped thin film can be ascertained from the shift in the position of the ω_0 phonon mode from ~615 cm^{-1} for the pure VO_2 to ~629 cm^{-1} for the Cr-doped thin film, which also shows a characteristic shoulder at ~575 cm^{-1} [7,26].

The correct chemical state of vanadium present in the pure and Cr-doped VO_2 thin films has been confirmed by the XPS measurements. Figures 2(a) and 2(b) show that vanadium is present in the +4 oxidation state in both pure and Cr-doped thin films, which is evident from the binding energy values of spin-orbit split features, i.e., V $2p_{3/2}$ ~ 515.6 eV and V $2p_{1/2}$ ~ 523.1 eV [27]. The small intensity of the OH feature at ~531.3 eV indicates the clean surface of the thin film, and a peak at ~530 eV corresponds to the O 1s feature. There is not much notable difference observed from the respective spectra of pure and Cr-doped thin films, except a slightly lower value of the integrated intensity of V^{4+} in the Cr-doped thin film due to lower vanadium content. The feature marked S is assigned as the satellite peak of V $2p_{3/2}$ [28]. Slightly higher binding energy values of V $2p_{3/2}$ and V $2p_{1/2}$ in the doped thin film with respect to the pure thin film are consistent with previous studies [29]. The spectrum also reveals that the Cr has been doped in the +3 oxidation state, which is visible from the binding energy values of Cr $2p_{3/2}$ ~ 577.3 eV and $2p_{1/2}$ ~ 586.7 eV [see the inset of the Fig. 2(a)] [30]. This indicates some oxygen deficiency in the Cr-doped VO_2. The precise Cr content was calculated from XPS spectra, confirming an ~1.5% Cr concentration. Feature A in the V 2p XPS spectrum of the Cr-doped VO_2 is absent in the pure VO_2 and is assigned to the $V^{1+/2+}$ oxidation state, arising from the reduction of some of the V^{4+} ions due to the oxygen deficiency created by the Cr doping [28].

Figure 3(a) shows temperature-dependent four-point-probe resistivity measurements. Both films undergo a first-order insulator-to-metal transition, as evidenced by hysteresis loops during the resistivity change. The pure film exhibits an IMT transition at ~336.19 K, while the Cr-doped one exhibits one at ~331.34 K. Both transition temperatures are lower

TABLE I. Parameters obtained from the fittings of the $d\ln R/dT$ vs temperature data of the pure and Cr-doped VO_2 thin films.

Sample	T_c (K)	ΔH (K)	ΔT (K)
VO_2	336.19	10.05	5.79
Cr-VO_2	331.34	8.7	7.65
VO_2 [34]	338.5	5.0	2.6
VO_2 [33]	343.2	4.8	8.5

than that of the bulk VO_2 (341 K) [31]. The lowering of the transition temperature for the Cr-doped film contradicts earlier resistivity measurements for the bulk, where the Cr substitution in VO_2 caused an increase in the IMT transition temperature [3,32]. Since both films were grown under identical deposition conditions, the decrease in transition temperature by ∼5 K of the doped film compared to the pure compound may be because of the effect of Cr doping in the strained situation, as strain is inevitable in thin films. To characterize the IMT, a Gaussian curve was used for fitting the differential curves of $\ln(R)$ vs T heating and cooling cycles, as shown in Fig. 3(b). Values of T_c (transition temperature), ΔH (hysteresis width), and ΔT (transition sharpness) are listed in the Table I along with previous reported values for the VO_2 thin film on different substrates [33,34]. Smaller T_c and larger ΔH in our samples reflect a stronger effect of the strain on the IMT as described by the Clausius-Clapeyron equation [15,35]. The strain estimated in our VO_2 thin film amounts to ∼0.542%. It is calculated using the (011) reflection and has a compressive nature. The higher value of the resistivity in the Cr-doped VO_2 is consistent with earlier reports [32].

Figures 4(a) and 4(b) show temperature-dependent Raman measurements of the pure and Cr-doped VO_2 thin films, respectively. According to group theory, the $M1$ phase of VO_2 has 18 Raman active modes (9 A_g and 9 B_g), out of which 12 modes are identified at ∼140, 193, 223, 261, 308, 338, 387, 395, 440, 497, 614, and 820 cm^{-1} [36]. The Raman mode observed at ∼520 cm^{-1} is from the Si substrate. Isotopic substitution and density functional theory calculations have assigned the low-frequency A_g phonons ω_{v_1} (193 cm^{-1}) and ω_{v_2} (223 cm^{-1}) to V-V lattice motion, with ω_{v_1} involving the twisting vibration of V-V dimers. All other distinguishable peaks are related to V-O vibrations [26]. A blueshift in the V-O vibration (ω_0) at ∼615 cm^{-1} is a fingerprint of the VO_2 insulating phases ($M2$ and T) [25,36]. Group theory predicts the same number of Raman modes for the $M2$ and T structures as predicted for the $M1$ structure. At room temperature (RT) phonon modes observed in the Cr-doped VO_2 thin film belong to the triclinic T phase of VO_2 evident from the position of the strongest ω_0 vibration at ∼629 cm^{-1}, in agreement with the literature [7,9,26,37].

Temperature-dependent Raman measurements reveal a structural transition from the monoclinic $M1$ structure to the rutile R structure in the pure VO_2 thin film [see Figs. 4(a) and 4(c)], while the Cr-doped VO_2 thin film has an intermediate Mott monoclinic $M2$ structure between the RT T structure and the high-temperature rutile R structure, as evidenced by a

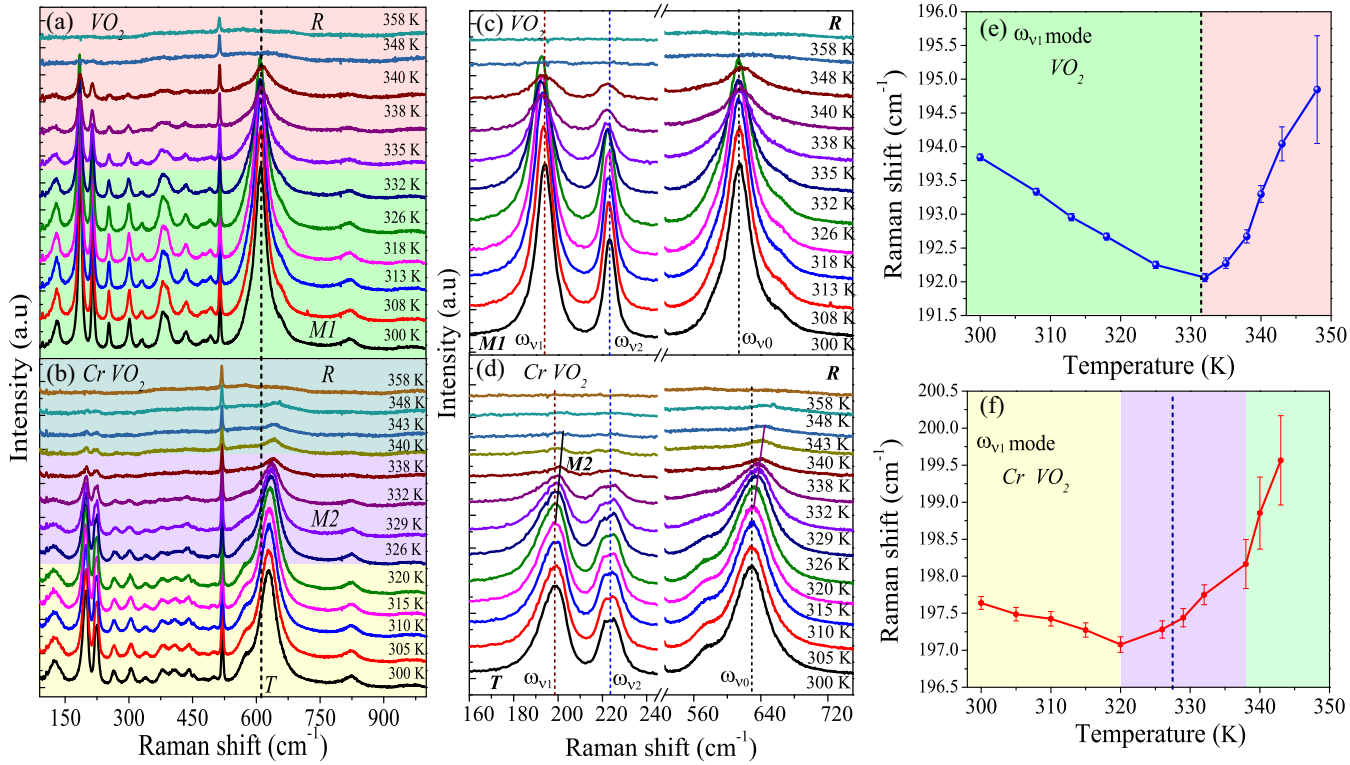

FIG. 4. Temperature-dependent Raman spectra of (a) pure and (b) Cr-doped VO_2 thin films collected in the cooling cycles. Zoomed-in view of selected phonon modes (ω_{v_1}, ω_{v_2}, and ω_0) of (c) pure and (d) Cr-doped VO_2 thin films. Temperature-dependent frequency shift of the ω_{v_1} Raman mode positions obtained from Lorentz fitting of this mode in (e) pure and (f) Cr-doped VO_2 thin films in the cooling cycle. Dotted vertical lines indicate the IMT temperature from resistivity measurements in the cooling process.

blueshift in the position of the ω_0 vibration from ~629 cm^{-1} at RT to ~642 cm^{-1} at ~329 K, as shown in Figs. 4(b) and 4(d) [7,25,26,36]. Measurements presented here are from the cooling cycles, and similar behavior is expected in the heating cycles, except with slightly higher transition temperatures T_s due to the first-order nature of the transition.

Structural transition from the monoclinic structure to the rutile structure in the pure VO_2 occurs at $T_s \sim 336$ K, which is evident from the temperature-dependent integrated intensity of the ω_{v_1} frequency mode, as shown in Fig. 3(c). To further evaluate the temperature-dependent structural rearrangements in the pure and Cr-doped thin films we plot temperature-dependent frequency shifts of the Raman frequency ω_{v_1} obtained by Lorentzian fitting of the phonon modes from the data in the cooling cycle in Figs. 4(e) and 4(f). The monoclinic $M1$ and $M2$ and triclinic T structures of VO_2 differ in arrangement of the vanadium atoms along the c axis. Structural rearrangements among the vanadium atoms are visible in the frequency shift of ω_{v_1} with temperature. The softening of the ω_{v_1} phonon vibration in the pure thin film observed up to the structural transition temperature is due to thermal expansion of lattice. However, above T_s, an abrupt hardening of the ω_{v_1} vibration is seen which is attributed to structural transformation of the monoclinic $M1$ phase to the rutile R structure. In the Cr-doped thin film, thermal effects are seen up to ~318 K (below T_c), above which the slow hardening of the phonon mode is observed. This confirms that structural rearrangement is taking place inside the lattice which is attributed to transformation of the T phase into the intermediate $M2$ monoclinic phase, which finally gets transformed into the rutile R metallic phase above ~338 K evident from the steep hardening of the Raman mode. From temperature-dependent Raman spectra of both thin films, cophasing can be visualized in broad structural transitions [38]. Due to cophasing and broad structural transitions in these films it is not possible to define sharp structural transition boundaries. Vertical dashed lines in Figs. 4(e) and 4(f) represent the IMT temperatures of the thin film, obtained from resistivity measurements in the cooling cycles.

Ultrafast pump-probe reflectivity measurements are performed to understand the photoinduced carrier dynamics in both thin films. Time-resolved photoinduced measurements of the differential reflectivity ($\Delta R/R$) of pure ($M1$ phase) and Cr-doped (T phase) VO_2 thin films are shown in Fig. 5. The photon energy of our experiment, ~1.56 eV, corresponds to the transition from the electron-occupied valence $3d_{\|}$ to the $\pi^\star$ band (resulting from the hybridization among V $3d$ and O $2p$ orbitals) [39]. Figure 5(a) shows the normalized differential reflectivity curves for the pure and Cr-doped VO_2 thin films at 315 and 310 K, respectively, at a fluence of 0.075 mJ/cm^2. The selected temperatures (315 and 310 K) are chosen to be 5 K apart because their IMT temperatures also differ by ~5 K. The initial rise in $\Delta R/R$ is followed by an exponential decrease. The initial fast increase in $\Delta R/R$ is attributed to the excitation of hot electrons from the valence band to the conduction band by a pump pulse. The dynamics of charge carriers is explained on the basis of the two-temperature model, which indicates that the elastic and inelastic scatterings that occur among different carriers (electrons and holes) randomize their momenta and thermalize them to an internal equilibrium temperature T_e significantly higher than the phonon temperature T_l acquired with the fast-relaxation process. In the slow-electron-relaxation process, the effective electron temperature decreases as the electron system transfers energy to the lattice via inelastic electron-phonon interactions [40–42]. We have fitted our experimental data with the biexponential model that describes a set of decaying exponential functions, representing different electron-relaxation mechanisms, formulated as

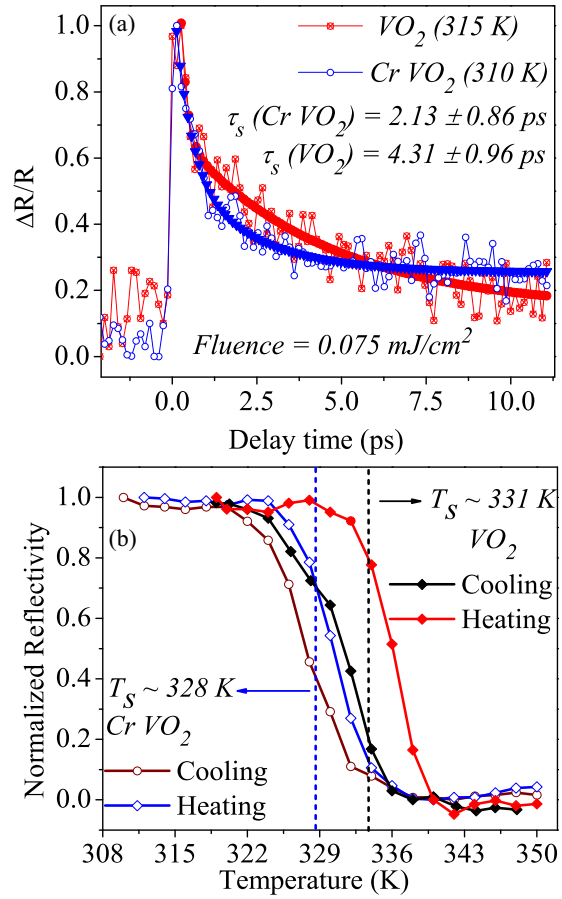

FIG. 5. (a) Biexponential fits of time-resolved reflectivity measurements in the pure and Cr-doped VO_2 thin films at 315 and 310 K. (b) Normalized reflectivity of doped and pure VO_2 thin films.

$$\frac{\Delta R}{R} = F_1 e^{\frac{-t}{\tau_f}} + F_2 e^{\frac{-t}{\tau_s}} + F_3, \tag{1}$$

where $F_1(\tau_f)$, $F_2(\tau_s)$ represent the amplitudes of the fast- and slow-electron-relaxation processes and F_3 represents the extremely long-lived component. The slow relaxation time τ_s values for the pure (4.31 ± 0.96 ps) and Cr-doped (2.13 ± 0.86 ps) VO_2 thin films indicate the different dynamics of the slow-electron-relaxation process. Relaxation time may also have contributions from the microstructures of the thin film and their role in the kinetics of the excited state and/or any metastable phase that may occur during decay [43,44]. In the present case, since both films were grown under identical conditions, the considerable difference in the slow relaxation time may be attributed directly to the uniqueness of the vanadium dimerizations in the $M1$ and T phases.

To elaborate on and describe the nature of the IMT through transient reflectivity and to estimate the laser heating effect, temperature-dependent normalized reflectivity at a negative

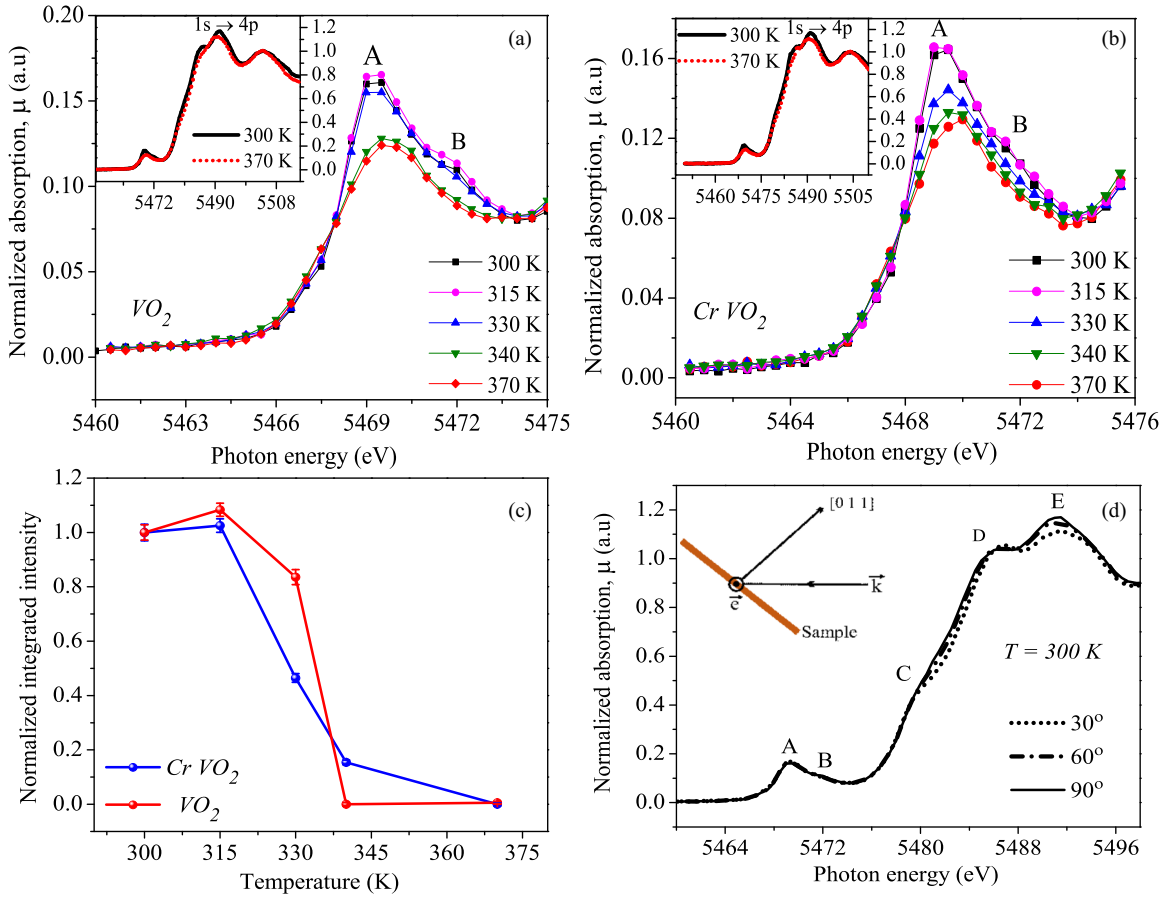

FIG. 6. Temperature dependence of XANES pre-edge features of the V K edge measured in the cooling cycles for (a) pure and (b) Cr-doped VO_2 thin films. Insets: Normalized K-edge XANES spectra of (a) pure and (b) Cr-doped VO_2 thin films. (c) Normalized temperature-dependent integrated intensity of feature A in (a) and (b) in the cooling cycle. (d) Room-temperature angle-dependent K-edge XANES spectra for VO_2 thin film. Angles are between the photon's polarization vector $\vec{e}$ and the [011] (surface-normal) axis of the sample.

pump-probe delay time of 400 fs (where the thermal effects of the laser beam are minimum) is shown in Fig. 5(b). The observation of hysteresis confirms the first-order nature of the transition in the normalized reflectivity that occurs at ∼333 and ∼328 K in pure and Cr-doped thin films, respectively. The lower value of the transition temperatures (∼5 K) obtained here for both thin films compared to resistivity and Raman measurements may be attributed to the laser heating of thin films. Further, the details of the fluence and temperature-dependent transient reflectivity measurements for these films are provided in the Supplemental Material [45].

The temperature-dependent pre-edge features of the vanadium K-edge XANES of the pure and Cr-doped VO_2 thin films are illustrated in Figs. 6(a) and 6(b). The insets show the complete XANES spectra for the respective samples. The strong absorption peak at ∼5491.2 eV is assigned to the dipole allowed V 1s to 4p transitions. The pre-edge peak at ∼5469.2 eV corresponds to the dipole-forbidden transition from the V 1s core level to the 3d states. The pre-edge absorption in VO_2 becomes allowed due to the overlapping of the V 3d orbitals with the V 4p and O 2p orbitals. The energy positions of the pre-edge and main absorption peaks are related to the oxidation states of the vanadium according to Kunzl's law [46]. In our films, the energy positions match very well with those reported for bulk VO_2, confirming the +4 oxidation of vanadium in both pure and Cr-doped thin films, which is in agreement with our XPS data.

In general, the pre-edge peak intensity is highly sensitive to the local geometrical structure around the absorbing atom (V). The intensity of the pre-edge peak increases with the deviation from regular octahedral VO_6 units such as VO (virtually zero intensity) to VO_2, where the symmetry of the ligands is decreased [47]. Temperature-dependent pre-edge intensity variation in the pure and Cr-doped VO_2 thin films presented in Figs. 6(a) and 6(b) shows that the observed intensity of the pre-edge feature in both thin films decreases on going from the insulating monoclinic $M1$ and triclinic T to the metallic rutile R state. This indicates a less distorted octahedron in the rutile metallic state compared to the monoclinic and triclinic insulating states. The pre-edge feature contains two structures, A and B, corresponding to the crystal-field-split V 3d states, i.e., t_{2g} and e_g, respectively [48]. The intensity of pre-edge feature B has been found to be very sensitive to the VO_2 octahedral distortion, having a large intensity in the distorted insulating phase. The normalized integrated intensity of feature A in the cooling cycle from 370 K to RT is shown in Fig 6(c). A sharp transition is observed in the pure VO_2 thin film at the IMT, while a broad transition and

a significant nonvanishing feature A intensity are observed in the Cr-doped thin film. This nonvanishing behavior of the feature A intensity in the Cr-doped VO_2 is attributed to the intermediate VO_2 $M2$ phase already visualized from the Raman spectroscopy.

Figure 6(d) shows the room-temperature XANES measured at different orientations between the surface normal of the thin film and the electric field vector of the incident beam. An appreciable increase in the intensity of feature C and main edge feature E is observed on changing angle between the surface normal and the electric field vector of incident photons. These observations are consistent with the results reported earlier for single-crystal VO_2 [49] and indicate that although these thin films are polycrystalline in nature, all the crystallites share common surface normal vectors. The details of the angle-dependent XANES in the insulating and metallic phases of both the pure and Cr-doped VO_2 along with the XANES of the V foil (used for energy calibration) are given in the Supplemental Material [45].

IV. DISCUSSION AND CONCLUSIONS

In the following we will discuss the main result of the paper, which is about the electronic structure of the VO_2 insulating phases. Figure 7(a) shows the electronic structure, t_{2g} and e_g features, in the pre-edge part of the vanadium K-edge XANES of the insulating $M1$ and T and metallic R phases of the pure and Cr-doped VO_2 thin films. These features of the respective insulating phases ($M1$ and T) as well as the metallic phase (R) of both thin films are almost identical. Identical electronic structures of the $M1$ (pure VO_2) and T (Cr-doped VO_2) phases are incompatible with the Peierls model. To completely understand the nature of the electronic structures of all the insulating phases ($M1$, T, and $M2$) observed in these thin films, we have also extracted the electronic structure of the $M2$ phase from the temperature-dependent XANES at the specified temperatures using the linear combination approach. The spectrum at the temperatures where cophasing is observed can be expressed as the linear combination of the monoclinic ($M2$) and rutile (R) phases as follows:

$$\mu_{\text{measured}} = m_2\mu_{M2} + r\mu_R, \tag{2}$$

where m_2 and r are the phase fractions of the $M2$ and R phases. At a temperature of 331 K (near the inflection point in the resistivity measurements), using a phase fraction of ~50% each for the $M2$ and R phases, estimated from the temperature-dependent Raman spectra, the electronic structure of the $M2$ phase was extracted [$\mu_{M2} = \frac{\mu_{\text{measured}} - r\mu_R}{m_2}$, from Eq. (2)] and is shown in Fig. 7(b). It is notable that the electronic structures of the insulating $M1$, T, and $M2$ phases are found identical, irrespective of their different structural arrangements. This is clear evidence that $M1$, T, and $M2$ insulating phases firmly lie in the Mott-Hubbard limit ($U \gg t$) [2,10]. In order to further substantiate this observation we have also extracted the $M2$ phase electronic structure at other temperatures (315 and 341 K) and compared the results with $M1$ and T phase electronic structures (see the Supplemental Material [45]). We find that $M2$ spectra at other temperatures are also identical to $M1$ and T phase spectra.

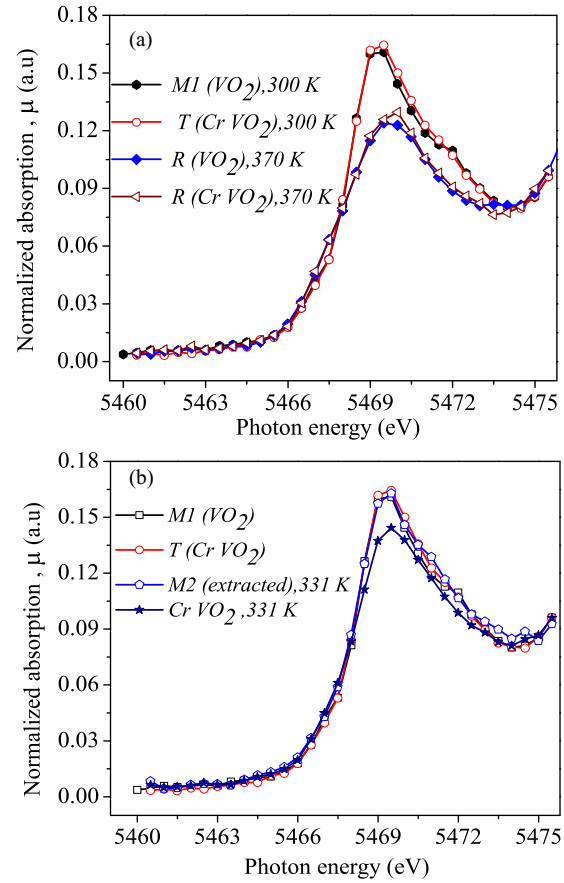

FIG. 7. (a) Electronic structures of the room-temperature insulating monoclinic $M1$ and triclinic T phases and the high-temperature rutile R phases in the respective samples. (b) Electronic structure of the extracted $M2$ phase using the linear combination approach [Eq. (2)] at 331 K, the experimental spectrum at 331 K of the Cr-doped VO_2 thin film, and spectra of the other two insulating phases ($M1$ and T).

Conventionally, in a Mott-Hubbard insulator valence electrons are localized on the individual ions, while in the insulating phases of VO_2 (with different dimerizations) the dimerized chains contain covalently bonded singlets which are localized on the vanadium dimers. This situation has made it difficult to distinguish between the Peierls and Mott-Hubbard pictures for many of the probes. For example, nuclear magnetic resonance (NMR) has already established the $M2$ phase as the Mott-Hubbard insulator phase, which is evident from the presence of the localized vanadium d electrons on the unpaired vanadium atoms (the hallmark of the Mott-Hubbard insulator); however, the NMR signal remains ambiguous in the dimerized phases ($M1$ and T). Our results show that the $M2$ phase has an electronic structure essentially identical to that of the other two insulating phases, and the $M2$ phase having been established as the Mott phase [9,11] clearly indicates that the other two phases ($M1$ and T) are also Mott-Hubbard insulators. Our observations are consistent with recent results [10] where, using optical broadband spectroscopy, the authors showed that the $M2$ and T phases are Mott-Hubbard insulators.

In conclusion, we have confirmed the growth of the monoclinic $M1$ and triclinic T phases in the pure and Cr-doped VO_2 thin films, respectively. The monoclinic $M2$ phase has been found in Cr-doped VO_2 at temperatures intermediate between the room-temperature triclinic T phase and the high-temperature rutile R phase. The characteristic insulator-to-metal transition observed in both thin films has been studied with structural, electrical, electronic structure, and ultrafast pump-probe techniques. In spite of different vanadium dimerizations in all three insulating VO_2 phases ($M1$, T, and $M2$) we experimentally find that the electronic structures of these phases are identical, confirming that these structural phases are the Mott-Hubbard insulators. Our study and approach are relevant to a broader class of correlated electron systems in which electronic correlations and structural degrees of freedom are entangled.

ACKNOWLEDGMENTS

The authors are grateful to S. Karwal and A. Rathore for help during XPS and Raman measurements, respectively. The authors are also grateful to J. Jayabalan and R. Chari for help and support during TR measurements. D.K.S. acknowledges support from DST and SERB, India, in the form of an inspire faculty award and an early-career research award (ECR/2017/000712). Parts of this research were carried out at PETRA III at DESY, a member of the Helmholtz Association (HGF).

[1] A. Zylbersztejn and N. F. Mott, Phys. Rev. B **11**, 4383 (1975).
[2] M. Imada, A. Fujimori, and Y. Tokura, Rev. Mod. Phys. **70**, 1039 (1998).
[3] M. Marezio, D. B. McWhan, J. P. Remeika, and P. D. Dernier, Phys. Rev. B **5**, 2541 (1972).
[4] D. B. McWhan, M. Marezio, J. P. Remeika, and P. D. Dernier, Phys. Rev. B **10**, 490 (1974).
[5] J. Zhou, Y. Gao, Z. Zhang, H. Luo, C. Cao, Z. Chen, L. Dai, and X. Liu, Sci. Rep. **3**, 3029 (2013).
[6] E. Sakai, K. Yoshimatsu, K. Shibuya, H. Kumigashira, E. Ikenaga, M. Kawasaki, Y. Tokura, and M. Oshima, Phys. Rev. B **84**, 195132 (2011).
[7] J. M. Atkin, S. Berweger, E. K. Chavez, M. B. Raschke, J. Cao, W. Fan, and J. Wu, Phys. Rev. B **85**, 020101 (2012).
[8] J. P. Pouget, H. Launois, J. P. D'Haenens, P. Merenda, and T. M. Rice, Phys. Rev. Lett. **35**, 873 (1975).
[9] J. Pouget, H. Launois, T. Rice, P. Dernier, A. Gossard, G. Villeneuve, and P. Hagenmuller, Phys. Rev. B **10**, 1801 (1974).
[10] T. J. Huffman, C. Hendriks, E. J. Walter, J. Yoon, H. Ju, R. Smith, G. L. Carr, H. Krakauer, and M. M. Qazilbash, Phys. Rev. B **95**, 075125 (2017).
[11] T. M. Rice, H. Launois, and J. Pouget, Phys. Rev. Lett. **73**, 3042 (1994).
[12] L. Yeo, A. Srivastava, M. Majidi, R. Sutarto, F. He, S. Poh, C. Diao, X. Yu, M. Motapothula, S. Saha *et al.*, Phys. Rev. B **91**, 081112 (2015).
[13] T. C. Koethe, Z. Hu, M. W. Haverkort, C. Schüßler-Langeheine, F. Venturini, N. B. Brookes, O. Tjernberg, W. Reichelt, H. H. Hsieh, H.-J. Lin *et al.*, Phys. Rev. Lett. **97**, 116402 (2006).
[14] N. B. Aetukuri, A. X. Gray, M. Drouard, M. Cossale, L. Gao, A. H. Reid, R. Kukreja, H. Ohldag, C. A. Jenkins, E. Arenholz *et al.*, Nat. Phys. **9**, 661 (2013).
[15] S. Majid, D. Shukla, F. Rahman, K. Gautam, R. Choudhary, V. Sathe, and D. Phase, Appl. Phys. Lett. **110**, 173101 (2017).
[16] D. Ruzmetov and S. Ramanathan, *Thin Film Metal Oxides: Fundamentals and Applications in Electronics and Energy* (Springer, New York, 2010).
[17] S.-K. Mo, J. D. Denlinger, H.-D. Kim, J.-H. Park, J. W. Allen, A. Sekiyama, A. Yamasaki, K. Kadono, S. Suga, Y. Saitoh *et al.*, Phys. Rev. Lett. **90**, 186403 (2003).
[18] S. Lysenko, A. Rúa, V. Vikhnin, F. Fernández, and H. Liu, Phys. Rev. B **76**, 035104 (2007).
[19] S. Wall, L. Foglia, D. Wegkamp, K. Appavoo, J. Nag, R. F. Haglund, Jr., J. Stähler, and M. Wolf, Phys. Rev. B **87**, 115126 (2013).
[20] J. Lourembam, A. Srivastava, L. Cheng, T. Venkatesan, E. E. Chia *et al.*, Sci. Rep. **6**, 25538 (2016).
[21] C. Kübler, H. Ehrke, R. Huber, R. Lopez, A. Halabica, R. F. Haglund, Jr., and A. Leitenstorfer, Phys. Rev. Lett. **99**, 116401 (2007).
[22] S. Khan, J. Jayabalan, R. Chari, S. Pal, S. Porwal, T. K. Sharma, and S. Oak, Appl. Phys. Lett. **105**, 073106 (2014).
[23] J. Strempfer, S. Francoual, D. Reuther, D. K. Shukla, A. Skaugen, H. Schulte-Schrepping, T. Kracht, and H. Franz, J. Synchrotron Radiat. **20**, 541 (2013).
[24] B. Ravel and M. Newville, J. Synchrotron Radiat. **12**, 537 (2005).
[25] K. Okimura, N. H. Azhan, T. Hajri, S.-i. Kimura, M. Zaghrioui, and J. Sakai, J. Appl. Phys. **115**, 153501 (2014).
[26] C. Marini, E. Arcangeletti, D. Di Castro, L. Baldassare, A. Perucchi, S. Lupi, L. Malavasi, L. Boeri, E. Pomjakushina, K. Conder *et al.*, Phys. Rev. B **77**, 235111 (2008).
[27] G. Silversmit, D. Depla, H. Poelman, G. B. Marin, and R. D. Gryse, J. Electron. Spectrosc. Relat. Phenom **135**, 167 (2004).
[28] R. Zimmerman, R. Claessen, F. Reinert, P. Steiner, and S. Hüfner, J. Phys. Condens. Matter **10**, 5697 (1998).
[29] L. F. J. Piper, A. DeMasi, S. W. Cho, A. R. H. Preston, J. Laverock, K. E. Smith, K. G. West, J. W. Lu, and S. A. Wolf, Phys. Rev. B **82**, 235103 (2010).
[30] V. Maurice, S. Cadot, and P. Marcus, Surf. Sci. **458**, 195 (2000).
[31] F. J. Morin, Phys. Rev. Lett. **3**, 34 (1959).
[32] A. Rúa, R. Cabrera, H. Coy, E. Merced, N. Sepúlveda, and F. E. Fernández, J. Appl. Phys. **111**, 104502 (2012).
[33] T.-H. Yang, R. Aggarwal, A. Gupta, H. Zhou, R. J. Narayan, and J. Narayan, J. Appl. Phys. **107**, 053514 (2010).
[34] Y. Ji, T. Pan, Z. Bi, W. Liang, Y. Zhang, H. Zeng, Q. Wen, H. Zhang, C. Chen, Q. Jia *et al.*, Appl. Phys. Lett. **101**, 071902 (2012).
[35] J. Cao, E. Ertekin, V. Srinivasan, W. Fan, S. Huang, H. Zheng, J. Yim, D. Khanal, D. Ogletree, J. Grossmanan *et al.*, Nat. Nanotechnol **4**, 732 (2009).

[36] Y. Ji, Y. Zhang, M. Gao, Z. Yuan, Y. Xia, C. Jin, B. Tao, C. Chen, Q. Jia, and Y. Lin, Sci. Rep. **4**, 4854 (2014).
[37] T. Huffman, P. Xu, M. Qazilbash, E. Walter, H. Krakauer, J. Wei, D. Cobden, H. Bechtel, M. Martin, G. Carr *et al.*, Phys. Rev. B **87**, 115121 (2013).
[38] X.-B. Chen, J.-H. Shin, H.-T. Kim, and Y.-S. Lim, J. Raman Spectrosc. **43**, 2025 (2012).
[39] D. Ruzmetov, S. D. Senanayake, and S. Ramanathan, Phys. Rev. B **75**, 195102 (2007).
[40] X. Zou, D. Zhan, X. Fan, D. Lee, S. K. Nair, L. Sun, Z. Ni, Z. Luo, L. Liu, T. Yu *et al.*, Appl. Phys. Lett. **97**, 141910 (2010).
[41] S. Wang, J. G. Ramírez, J. Jeffet, S. Bar-Ad, D. Huppert, and I. K. Schuller, Europhys. Lett. **118**, 27005 (2017).
[42] R. H. M. Groeneveld, R. Sprik, and A. Lagendijk, Phys. Rev. B **51**, 11433 (1995).
[43] X. Xue, M. Jiang, G. Li, X. Lin, G. Ma, and P. Jin, J. Appl. Phys. **114**, 193506 (2013).
[44] M. Nakajima, N. Takubo, Z. Hiroi, Y. Ueda, and T. Suemoto, Appl. Phys. Lett. **92**, 011907 (2008).
[45] See Supplemental Material at http://link.aps.org/supplemental/10.1103/PhysRevB.98.075152 for angle-dependent XANES measurements, phase fraction estimate, and transient reflectivity data for fluence and temperature change.
[46] C. Mande and V. B. Sapre, in *Advances in X-ray Spectroscopy*, edited by C. Bonnelle and C. Mande (Pergamon, New York, 1983), Chap. 17, pp. 287–301.
[47] J. Wong, F. W. Lytle, R. P. Messmer, and D. H. Maylotte, Phys. Rev. B **30**, 5596 (1984).
[48] A. Bianconi, Phys. Rev. B **26**, 2741 (1982).
[49] B. Poumellec, R. Cortes, E. Loisy, and J. Berthon, Phys. Status Solidi B **183**, 335 (1994).